

A Convolutional Persistence Transform

Elchanan Solomon

Department of Mathematics, Duke University
Durham, USA
elchanansolomon@gmail.com

Paul Bendich

Department of Mathematics, Duke University
Geometric Data Analytics
Durham, USA
paul.bendich@duke.edu

Abstract—We consider a new topological featurization of d -dimensional images, obtained by convolving images with various filters before computing persistence. Viewing a convolution filter as a motif within an image, the persistence diagram of the resulting convolution describes the way the motif is distributed throughout that image. This pipeline, which we call *convolutional persistence*, extends the capacity of topology to observe patterns in image data. Indeed, we prove that (generically speaking) for any two images one can find *some* filter for which they produce different persistence diagrams, so that the collection of all possible convolutional persistence diagrams for a given image is an injective invariant. This is proven by showing convolutional persistence to be a special case of another topological invariant, the Persistent Homology Transform. Other advantages of convolutional persistence are improved stability and robustness to noise, greater flexibility for data-dependent vectorizations, and reduced computational complexity for convolutions with large stride vectors. Additionally, we have a suite of experiments showing that convolutions greatly improve the predictive power of persistence on a host of classification tasks, even if one uses random filters and vectorizes the resulting diagrams by recording only their total persistences.

I. INTRODUCTION

Persistent homology is a method of assigning multiscale topological descriptors to parametric families of shapes. In *functional* persistence, the object of study is a real-valued function $f : X \rightarrow \mathbb{R}$ defined over a space X , and the parametric family of shapes are the sublevel-sets $X_\alpha = \{x \in X : f(x) \leq \alpha\}$. It is similarly possible to consider superlevel-sets, which is equivalent to negating the *filter function* f . One crucial feature of this construction is that X_α is a subset of X_β for $\alpha \leq \beta$, so that the sublevel-sets are naturally nested. The output of persistent homology is a collection of intervals (equivalently, a collection of points), called a *barcode* (or *persistence diagram*, using the point representation). The space of barcodes is not a vector space, even approximately [BW20, Wag21], but there do exist multiple *vectorizations* [AEK⁺17, Bub15, MKPGC19, DFF15, COO15] that transform barcodes into vectors suitable for machine learning and data analysis.

A very general setting for functional persistence is that of *simplicial complexes*, i.e. shapes obtained by gluing together

The authors were partially supported by the Air Force Office of Scientific Research under the grant “Geometry and Topology for Data Analysis and Fusion”, AFOSR FA9550-18-1-0266. They would also like to extend their thanks to Alexander Wagner, for helpful conversations.

points, edges, triangles, tetrahedra, etc. For example, if X is a triangulation of a 2D rectangular grid, a function $f : X \rightarrow [0, 1]$ can be viewed as a grayscale image. Persistent homology can then be understood as a feature extraction method for such images, either for supervised or unsupervised learning. Example applications include removing image noise [CD18, CDH22], parameter estimation for PDEs [CG21, AEK⁺17], segmentation [HLSC19], flow estimation [SMM⁺21], tumor analysis [CMC⁺20], cell immune micronenvironment [ACC⁺20], and materials science [HNN⁺16].

It should be understood that purely topological methods do not provide state-of-the-art predictive accuracy on most machine learning tasks, and are not to be considered as *alternatives* to more general methods like neural nets and kernel methods. Rather, topological methods provide *principled* and *interpretable* features that are different from those extracted by other methods, and can help improve the performance and utility of the entire pipeline, especially in settings where data is limited, see [KZWB22].

To that end, it is important to understand the properties of functional persistence and their role in machine learning. Here we consider some of the most salient properties:

- (Computational complexity) For a simplicial complex K with N simplices, computing persistence is $O(N^\omega)$, where ω is the matrix multiplication constant [MMS11]. This means that such persistence calculations scale poorly in the resolution of data, especially high-dimensional data, where doubling the resolution in \mathbb{R}^d results in a 2^d -fold increase in the number of simplices.
- (Stability) Persistent homology is stable to small perturbations of the input data, in that the distance between the barcodes for two functions f and g on a common space X is bounded by $\|f - g\|_\infty$. However, persistence is not stable to outliers, so images that look similar outside of a small fraction of pixels can produce wildly different barcodes.
- (Flexibility) There is a single persistence diagram to be associated with each pair (X, f) of space X and real-valued function f . This lack of additional parameters makes applying persistence straightforward, but can also be limiting in contexts where data-dependent featurizations are desired.

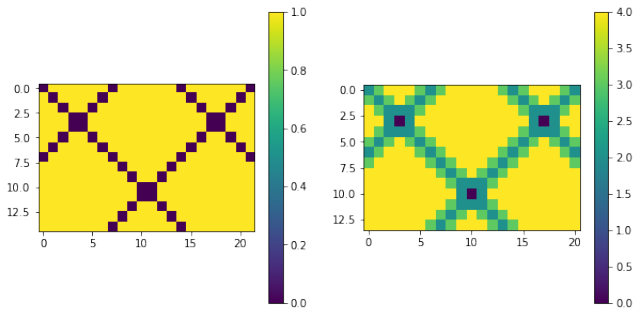


Fig. I.1: The original image is shown on the left. The image has interesting topological structure but the sublevel-set persistence is trivial. On the right, we show the result of convolving with a 2×2 -filter with a value of 1 in each pixel. The sublevel-set persistence of the convolved image is more informative; at height zero, there are three connected components, corresponding to three regions in the image where the convolution is zero. These regions then merge at an immediate value, due to those parts of the image where the local patches are more similar to the filter.

- (Invertibility) There exist many distinct space-function pairs (X, f) producing identical barcodes. Thus, persistence is not invertible as feature map, and this loss of information may hinder the capacity of persistence-based methods to identify patterns or distinguish distinct images.

Our goal in this paper is to introduce a modification to persistence of certain simplicial complexes that is (1) faster to compute, (2) more stable to outliers, (3) allows for data-driven tuning, (4) is provably invertible, and (5) is more informative in practice. Essentially, this technique consists of passing multiple convolutional filters over an image and computing the persistence of the resulting collection of low-resolution outputs. Since this pipeline consists principally of combining convolutions with persistence, we call it *convolutional persistence*. A crucial insight in this paper is that convolutional persistence can generically be transformed into a special case of the Persistent Homology Transform (PHT) [TMB14] in high-dimensions, implying that it shares the theoretical properties enjoyed by that invariant; see Section III-A for a definition of the PHT.

To get an intuitive sense for why convolutions might be of value in applied topology, consider Figure I.1, which shows how convolution with a simple filter makes geometric information in an image more available to topological methods.

A. Results

The major theoretical result of the paper is that convolutional persistence is generically injective (Theorem IV.7). We also provide stability and robustness results (Propositions IV.1 and IV.2), and corollaries that extend the injectivity result of

Theorem IV.7 to the multi-channel image setting (Corollary IV.11) and restrict the collection of convolutions needed to obtain injectivity (Corollary IV.10). The experimental results of Section V show that convolutional persistence significantly outperforms ordinary persistence at a collection of classification tasks, and also that it is more robust to the introduction of Gaussian noise. Interestingly enough, random filters perform well for the classification tasks considered, even when only the total persistences of the resulting diagrams are taken as feature vectors.

B. Overview

The remainder of the paper is organized as follows. Section II provides a thorough, non-technical survey on persistent homology. Section III defines *convolutional persistence* and reviews prior related work. Section IV contains the main theoretical results of the paper. Section V compares ordinary and convolutional persistence on a host of datasets, showing the capacity of convolutional persistence to produce features well-suited for image classification. Finally, Section VI discusses outstanding questions and potential generalizations of this work. Code for running experiments with convolutional persistence can be found at <https://github.com/yesolomon/convpers>.

II. BACKGROUND

The content of this paper assumes familiarity with the concepts and tools of persistent homology. Interested readers can consult the articles of Carlsson [Car09] and Ghrist [Ghr08] and the textbooks of Edelsbrunner and Harer [EH10] and Oudot [Oud15]. We include the following primer for readers interested in a high-level, non-technical summary.

A. Persistent Homology

Persistent homology records the way topology evolves in a parametrized sequence of spaces. In the case of functional persistence, we consider an ambient space X equipped with a real-valued function $f : X \rightarrow \mathbb{R}$. The sublevel-sets $X_\alpha = \{x \in X : f(x) \leq \alpha\}$ of f are naturally nested, in that X_α is a subset of X_β for $\alpha \leq \beta$, and these form a *filtration* of X . Persistence records how the topology of this filtration evolves as a function of the parameter α .

Simplicial complexes admit particularly simple filtrations. To every simplex σ we can associate a real value $f(\sigma)$ that encodes the parameter value at which it appears in the filtration of X . The only restriction on the function f is the following consistency condition: if σ is a sub-simplex of a higher-dimensional simplex τ (i.e. an edge which sits at the boundary of a triangle), we must have $f(\sigma) \leq f(\tau)$, ensuring that simplices do not appear before any of their faces.

Given a filtered simplicial complex, as the sequence of sublevel-sets evolves, the addition of certain edges or higher-dimensional simplices alters the *topological type* of the space. A precise way of quantifying topology is *homology*,

which measures the number of connected components (zero-dimensional homology), cycles (one-dimensional homology), or voids (higher-dimensional homology) in a space. Thus, homology can change when two connected components merge or a new cycle is formed. Simplices responsible for such topological changes are called *critical*. Persistent homology records the parameter values at which critical simplices appear, notes the dimension in which the homology changes, and pairs critical values by matching the critical value at which a new homological feature appears to the critical value at which it disappears. This information is then organized into a structure called a *barcode*, which is simply a collection of intervals. Figure II.1 shows the computation of the zero- and one-dimensional barcodes for a simple simplicial complex.

A barcode can also be encoded as a collection of points, simply by mapping each interval $[a, b]$ to the point $(a, b) \in (\mathbb{R} \cup \{-\infty\} \cup \{\infty\})^2$. This collection of points is called a *persistence diagram*, and besides for certain subtleties, such as dealing with open or closed endpoints and keeping track of points with multiplicity, it contains the exact same information as the original barcode. However, for certain analyses and vectorizations of persistence features, persistence diagrams are more useful than barcodes, as will be shown below.

When working with simplicial complexes, it is possible to limit the maximal dimension of simplices allowed in the construction. Given an arbitrary simplicial complex K , we write K^m to denote the subcomplex consisting of all simplices of dimension at most m ; this is called the *m-skeleton of K*. Note that K and K^m have the same homology in dimensions less than m , but may differ in dimension m , and K^m has no homology in dimension greater than m .

B. Image Cubical Complexes

A common alternative to simplicial complexes are *cubical complexes*, i.e. shapes that are built from vertices, edges, squares, cubes, etc. Such complexes are more natural when working with data built on top of a grid, such as pixel or voxel data, see [KMM04] for details. A cubical complex can always be converted into a simplicial complex by cutting up cubes into simplicial pieces: a canonical way of doing this is the *Freudenthal triangulation*. For a square, for example, this simply amounts to inserting a diagonal edge that produces two triangles. Given a function on a cubical complex, there is a canonical way to extend this function to its Freudenthal triangulation without changing its persistence; in the square example, in which the Freudenthal triangulation incorporates a diagonal edge and two triangles, we simply assign to these three simplices the filtration value assigned to the original square in the original cubical complex. Thus, from the perspective of persistence, it does not fundamentally matter if we work with cubical or simplicial complexes, although there is a difference vis-a-vis computations.

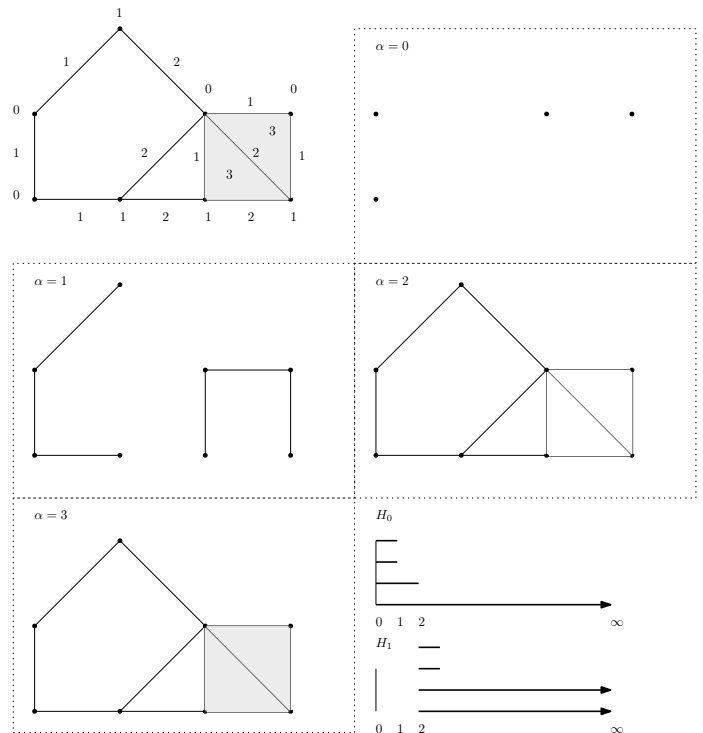


Fig. II.1: Top-left: A simplicial complex with filtration values attached to vertices, edges, and squares. Top-right through bottom-left: sublevel-sets associated with different threshold values. Bottom-right: barcodes in dimensions zero and one. The zero-dimensional homology H_0 barcode contains four bars, since at $\alpha = 0$ there are four connected components. Two bars die at $\alpha = 1$, since at that threshold value there are only two connected components. Finally, $\alpha = 2$ sees the merger of these connected components, so another bar dies at $\alpha = 2$ and the last persists to infinity. In one-dimensional homology H_1 , three bars are born at $\alpha = 2$, when three loops appear in the sublevel-set, and one of these bars dies at $\alpha = 3$, when that loop is killed off by the introduction of a square.

Given a d -dimensional grayscale image, there are two ways of turning this data into a cubical complex. One is to view the voxels as being vertices, and higher-dimensional cubes as coming from voxels adjacencies, so that pairs of adjacent pixels form an edge and squares come from four voxels in a square formation, etc. There is a canonical way of extending the function f from the voxels (vertices) to the entire complex: given a cube τ , define $f(\tau)$ to be $\max_{\sigma} f(\sigma)$, where the max is taken over all vertices $\sigma < \tau$. Thus, a square appears precisely once all its constituent vertices appear; this is called the *lower-** filtration.

Alternatively, one can also view the voxels as being d -dimensional cubes, and have the lower-dimensional cubes be the faces of these voxels. As before, there is a canonical way of extending the function value from the voxels (top-dimensional cubes) down to entire complex: for a cube σ ,

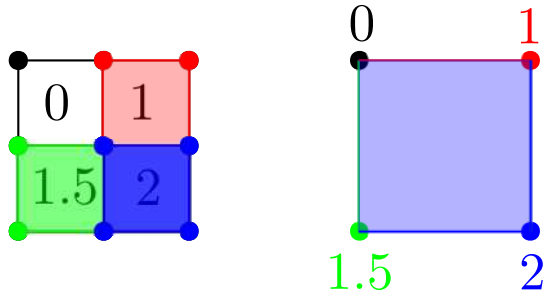


Fig. II.2: A 2×2 image can be turned into a complex in one of two ways. Left: A complex with four top-dimensional cubes, with function values, indicated using color, extended to vertices and edges via the upper-* rule. Right: A complex with four vertices, with function values extended to the edges and interior square via the lower-* rule.

define $f(\sigma)$ to be $\min_{\tau} f(\tau)$, where the min is taken over all voxels τ that contain σ . Thus, a cube appears precisely when at least one of the voxels in which it participates does; this is called the *upper-** filtration.

Consult figure II.2 for an illustration of these two images complexes. Generally, these complexes will differ, and the resulting persistence barcodes will be different. However, there exists a formula for reading the barcodes for one construction from the barcodes of the other, see [BGH⁺21].

C. Comparing Persistence Diagrams

As multi-sets of points in the plane, persistence diagrams are not vectors. However, there exist multiple metrics for comparing persistence diagrams. The most common approach is to view persistence diagrams as discrete distributions on the plane \mathbb{R}^2 , and use techniques from optimal transport theory, such as p -Wasserstein metrics W_p , to compare them, see [Oud17] Chapter 3 and [Vil21]. This analogy is complicated by the fact that persistence diagrams do not all have the same number of points, and that points in a persistence diagram near the diagonal line $y = x$ correspond to transient homological features, dying shortly after they are born, which ought not to play an important role in dictating similarity of diagrams. These problems are ameliorated by modifying the optimal transport protocol to allow pairing points in one diagram either with points in the other diagram or with the diagonal line $y = x$, the latter incurring a cost proportional to the distance of the given point from the diagonal. This *diagonal pairing* allows us to define an optimal transport distance between any pair of diagrams, regardless of how many points they have. In practice, the p -Wasserstein metrics in use are either $p = 1$, $p = 2$, or $p = \infty$, the latter of which is called the *Bottleneck distance* in persistence theory, and is written d_B . See Figure II.3 for a visualization of a matching between persistence diagrams.

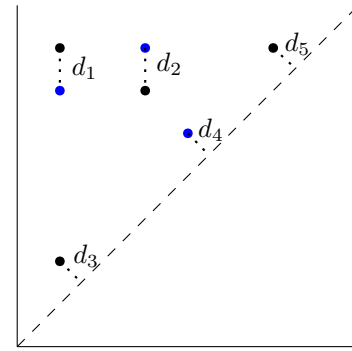


Fig. II.3: Two persistence diagram D_1 and D_2 , one in black and the other in blue. An optimal matching between these diagrams is shown, containing both diagonal and non-diagonal pairings. The resulting p -Wasserstein distance is then $W_p(D_1, D_2) = \sqrt[p]{d_1^p + d_2^p + d_3^p + d_4^p + d_5^p}$.

D. Computational Complexity

Persistence calculations are $O(N^\omega)$, where N is the number of simplices in the filtration and ω is the matrix multiplication constant [MMS11]. Though this bound is in practice quite pessimistic, it is accurate in reflecting the poor scaling of persistence calculations in the resolution of an image [OPT⁺17].

The bottleneck distance between persistence diagrams can be computed exactly using the well-known Hungarian algorithm, whose complexity is $O(n^3)$ for pairs of diagrams with at most n points. The number of points in the persistence diagram of filtration is always bounded by the total number N of simplices in the filtration, and may be much smaller. If one is interested in *approximating* the bottleneck, or more generally, p -Wasserstein distances between persistence diagrams, there are significantly faster methods than the Hungarian algorithm. One such method is based on *entropic approximation* techniques from optimal transport [LCO18], and provided that the norms of the points in the diagrams are uniformly bounded by some constant C , a transport plan within ϵ of the optimal matching can be produced in $O(\frac{n \log(n)C}{\epsilon^2})$ iterations of the Sinkhorn algorithm, which is itself linear in n .

E. Properties of Persistent Homology

Persistence theory guarantees that a small modification to the filtration of a space produces only small changes in its persistence diagram.

Theorem II.1 ([CSEH07]¹). *Let $f, g : X \rightarrow \mathbb{R}$ be two filtrations on a simplicial complex. Then the Bottleneck distance between their persistence diagrams is bounded by $\|f - g\|_\infty$.*

This implies that a small error in the filter function produces only small distortion in the resulting persistence

¹The main theorem of [CSEH07] is much more general, applying to tame functions on triangulable spaces, conditions which are automatically satisfied in the simplicial setting.



Fig. II.4: Two functions on the same grid with the same persistence, using either sublevel- or superlevel-set filtrations. Color scheme: {black: 0, grey: 0.5, white: 1}.

diagram. However, persistent homology is not at all stable to *outliers*, i.e. a small subset of the data having large error [BCD⁺14].

Recent work has established analogous stability results for W_p metrics between persistence diagrams. The latter of the following two results is particularly important for the subject matter of this paper.

Theorem II.2 ([ST20], Theorem 4.7). *Let $f, g : K \rightarrow \mathbb{R}$ be two functions on a fixed simplicial complex. Then for all $p \geq 1$,*

$$W_p(\text{Diag}(f), \text{Diag}(g)) \leq \|f - g\|_p.$$

Theorem II.3 ([ST20], Theorem 5.1). *Let $f, g : P \rightarrow \mathbb{R}$ be the grayscale functions for two images. Let \hat{f} and \hat{g} be the corresponding lower-* extensions to the d -dimensional cubical complex built on top of P , by either method described in Section II-B. Then we have the stability result:*

$$W_p(\text{Diag}(\hat{f}), \text{Diag}(\hat{g})) \leq \left(\sum_{i=1}^d 2^{d-i} \binom{d}{i} \right) \|f - g\|_p.$$

Another important feature of persistent homology is that the pipeline mapping a function f on a simplicial complex K , thought of as a vector in \mathbb{R}^K , to its associated persistence diagram is *almost everywhere differentiable* [GHO16, PSO18]. This is because the coordinates of the points in the diagram correspond to the values of f on critical simplices, and this correspondence is generically locally stable. However, large perturbations of f will change the location of critical simplices, as well as their pairings [BBW20], and non-differentiable nonlinearities can be found in those degenerate cases when the critical simplex data is not unique and locally unstable. This almost everywhere differentiability of persistent homology allows us to use gradient descent methods for topological optimization [CCG⁺21].

It is also important to note that persistent homology is not an injective invariant, meaning that different functions on the same space, or on different spaces, can have the same persistence diagrams [Cur18, LT21, LHP21], see Figure II.4. Thus, some information is lost in the process of converting a pair (X, f) to a persistence diagram.

We conclude the background section with an important lemma about the persistence of simplicial complexes embedded in Euclidean spaces. This lemma equates the persistence of two filtrations on such complexes, both extended from a function on the vertex set, one discretely (via the lower-* filtration) and the other continuously (via linear interpolation).

Proposition II.4. *Let K be an embedded simplicial complex in \mathbb{R}^d with vertex set K^0 . Given a function $f : K^0 \rightarrow \mathbb{R}$ we can extend this a function \hat{f} on K via the lower-* rule (so that it is constant on the interior of simplices). We can also extend f via linear interpolation, producing a function $f_* : K \rightarrow \mathbb{R}$. Then these two functions produce identical persistence diagrams, i.e. $\text{Diag}(K, f_*) = \text{Diag}(K, \hat{f})$.*

Proof. This follows from Lemma 2.3 of [BB97] and §VI.3 of [EH10]. \square

III. CONVOLUTIONAL PERSISTENCE

Our goal is to introduce a modification to functional persistence of cubical complexes based on the technique of *convolutions* in image processing. To that extent, we specialize to cubical complexes coming from integer grids. To be precise, let $P \subset \mathbb{Z}^d$ be a rectangle inside of the integer lattice, and let $f : P \rightarrow \mathbb{R}$ be a function defined on P . P can be viewed as the vertex set of an m -dimensional cubical complex K_P^m , and f can be extended to this complex via the lower-* rule, in which $f(\sigma) = \max_{p \in \sigma} f(p)$, as in Section II-B.

Definition III.1. Let $B \subset \mathbb{Z}^d$ be another rectangle, smaller than P , and let $g : B \rightarrow \mathbb{R}$ be a function on this rectangle; the pair (B, g) acts as a *convolutional filter*. Fix a vector $k = (k_1, \dots, k_d)$ with $k_i \in \mathbb{N}_{>0}$, corresponding to the *stride* of the convolution. For $v \in \mathbb{Z}^d$ with $B + (v \odot k) \subseteq P$,² define:

$$(g * f)(v) = \sum_{p \in B} g(p) f(p + v \odot k).$$

Let $R \subset \mathbb{Z}^d$ be the collection of values r such that $B + (r \odot k) \subseteq P$, which is necessarily also a rectangle. The pair $(R, g * f)$ is the output of our convolution. See Figure III.1.

Definition III.2. As a generalization of the above definition, we can allow n -channel images $f : P \rightarrow \mathbb{R}^n$ and filters $g : B \rightarrow \mathbb{R}^n$, in which case the above formula becomes:

$$(g * f)(v) = \sum_{p \in B} g(p) \cdot f(p + v \odot k).$$

Thus, the result of the convolution is real-valued (not vector valued), and ordinary persistent homology can be computed. In principle, it is possible to have the image and filter dimensions differ, and to compute the persistent of multi-channel images via *multiparameter persistence*, see [BL22], but this is beyond the scope of this work and presents its own set of theoretical and computational challenges.

²The symbol \odot refers to the Hadamard product, which performs componentwise multiplication between vectors.

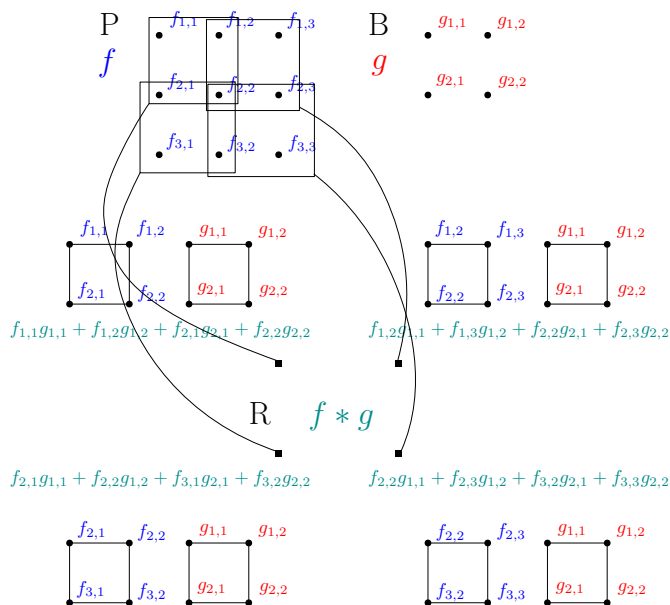


Fig. III.1: f is a function on a 3×3 grid P , with function values indicated by subscripts. g is a filter function on a 2×2 grid B . Using a stride vector $k = (1, 1)$, there are four possible translates of B that sit inside P , corresponding to the 2×2 grid R . Each vertex of R corresponds to a translate of B , and the value of $f * g$ at that vertex is obtained by lining up the values of g and f on that translate, multiplying them element-wise, and then summing them.

R may be much smaller than the support of f , since the various translates of B covering this support are not required to overlap much, if at all. In the degenerate setting where P and B are the same shape, R will consist of a single vertex. For the purposes of computing persistence, we will think of R , like P , as being the vertex set of a cubical complex K_R^m , and we extend functions on R to the entirety of the cubical complex using the lower-* rule.

Definition III.3. For a function f defined on the vertex set of a complex K , we write \hat{f} to denote its lower-* extension to all of K .

We propose that the collection of persistence diagrams of the form $PH(K_R^m, \widehat{g_i * f})$, for some set of filter functions $\mathcal{G} = \{g_i\}$, is of greater general utility than $PH(K_P^m, \hat{f})$. The computational advantages are immediate: when the stride k is large, so that R is much smaller than P , we have replaced a single, very expensive calculation with multiple, significantly faster calculations that can be performed in parallel. Moreover, we claim that this approach, which we deem *convolutional persistence*, is more robust and flexible than ordinary persistence, and has superior inverse properties. Proofs of robustness and injectivity can be found in the following Section IV.

The flexibility of convolutional persistence comes from

allowing the collection of filters \mathcal{G} to be curated for the task at hand. Indeed, there are many ways for this choice to be made:

- 1) Take \mathcal{G} to consist of a collection of popular filters in image processing, like blurring, sharpening, and boundary detection.
- 2) Take \mathcal{G} to consist of eigenfilters identified via PCA on the set of patches of images in the training set.
- 3) Picking filters *at random*.
- 4) Incorporate convolutional persistence in a deep learning pipeline and learn \mathcal{G} to minimize a chosen loss function.

In Section V, we compare some of these different choices on a range of data sets and learning tasks. We also demonstrate the stability of computational persistence experimentally.

We conclude this section with a simple complexity analysis. Given a d -dimensional grid P with p pixels of resolution in each direction, the total number of voxels $|P|$ is equal to p^d . Each voxel participates in a uniformly bounded number of higher-dimensional simplices, so the total number of simplices in the resultant complex is $O(p^d)$. Note that this is different from simplicial complexes built on top of point clouds, in which each point is allowed to create simplices with every other point; these non-local connections cause a further combinatorial explosion in the number of simplices. Thus, for functional persistence on grids, the total complexity of computing the persistence of a function on such a complex is $O(p^{d\omega})$, where ω is the matrix multiplication constant. When moving to convolutional persistence, the resolution shrinks when the stride is bigger than one. For a stride vector $k = (2, \dots, 2)$, the total number of voxels in the resulting grid R is $O((\frac{p}{2})^d)$, and hence the persistence calculations are $O((\frac{p}{2})^{d\omega})$, so that the complexity bound has decreased by a factor of $2^{d\omega}$. More generally, setting $\kappa = \prod_i k_i$, computing convolutional persistence for M filters has complexity $O(M \left(\frac{|P|}{\kappa}\right)^\omega)$. This means that, even computing convolutional persistence for a large class of filters, the speed-ups afforded by downsampling are significant. This was verified experimentally in [SWB21b], in the context of optimization of topological functionals.

A. Prior Work

Convolutional persistence is a type of *topological transform*, in which a parametrized family of topological invariants is associated to a fixed input. The first topological invariants studied were the *persistent homology transform* (PHT) and *Euler characteristic transform* (ECT) [TMB14]. In the same paper in which the PHT and ECT were defined, inverse theorems for provided; these theorems were generalized and extended by later work [CMT18, GLM18]. We will later show that convolutional persistence is, generically, a special case of the PHT, allowing us to take advantage of the inverse theory developed for that invariant. Invertible topological transforms have also been developed for weighted simplicial complexes [JKN20], metric graphs [OS17], metric spaces [SWB22], and metric measure spaces [MOS19]. Consult [OS20] for a more

thorough survey of inverse problem in applied topology.

Prior research has also studied the interaction of persistent homology and image convolutions. In [SWB21b], the authors use convolutions to stabilize and speed up topological optimization; the approach taken there can be viewed as a special case of convolutional persistence, in which the filter set \mathcal{G} consists of many random approximations of the box-smoothing filter. Unlike in this work, the goal of [SWB21b] is to produce many downsampled images with persistence similar to the original, permitting the computation of robust topological gradients. Another paper that considers both persistence and convolutions is [KKZ⁺20], where the authors develop a topological layer for deep learning models; one such model they consider is a convolutional neural network, and the authors design the network to compute topological features both before and after computing convolutions. However, [KKZ⁺20] do not study the interaction of convolutions and persistence in any generality.

IV. THEORETICAL RESULTS

In what follows, we fix an input domain P , filter region B and stride vector k , and a skeleton dimension m . Focusing on single-channel images, this determines the domain R for any convolutions of $f : P \rightarrow \mathbb{R}$ and $g : B \rightarrow \mathbb{R}$.

Proposition IV.1 (Stability). *Let $f_1, f_2 : P \rightarrow \mathbb{R}$ be two functions on P , and $g : B \rightarrow \mathbb{R}$ a filter function. Then, computing persistence over the complex K_R^m , for any $p \geq 1$ we have:*

$$\begin{aligned} & W_p(\widehat{\text{Diag}(f_1 * g)}, \widehat{\text{Diag}(f_2 * g)}) \leq \\ & \left(\sum_{i=1}^m 2^{m-i} \binom{m}{i} \right) \|g\|_1 \|f_1 - f_2\|_p \leq \\ |B| & \left(\sum_{i=1}^m 2^{m-i} \binom{m}{i} \right) \|g\|_\infty \|f_1 - f_2\|_p. \end{aligned}$$

Proof. Young's convolutional inequality (see [BR07], Chapter 3.9) states that for $p, q, r \geq 1$ with $\frac{1}{p} + \frac{1}{q} = \frac{1}{r} + 1$,

$$\|f * g\|_r \leq \|g\|_q \|f\|_p.$$

Setting $r = p$ forces $q = 1$, and setting $f = f_1 - f_2$, we obtain the bound $\|f_1 * g - f_2 * g\|_p \leq \|g\|_1 \|f_1 - f_2\|_p$. Since g is supported on a set of $|B|$ elements, we have $\|g\|_1 \leq |B| \|g\|_\infty$, so that $\|f_1 * g - f_2 * g\|_p \leq |B| \|g\|_\infty \|f_1 - f_2\|_p$. The bound then follows from Theorem II.3. \square

Proposition IV.2 (Robustness to Noise). *Fix a function $f : P \rightarrow \mathbb{R}$ and $g : B \rightarrow \mathbb{R}$ with $\|g\|_2 = 1$, and let $\tilde{f} = f + \epsilon$, where $\epsilon \sim \mathcal{N}(0, \sigma^2 I)$ models an independent normal in each voxel. Then:*

$$\begin{aligned} & \text{Prob}(W_\infty(\widehat{\text{Diag}(f * g)}, \widehat{\text{Diag}(\tilde{f} * g)}) \geq \alpha) \leq \\ & \frac{|R|\sigma}{\sqrt{\pi}\alpha} \exp\left(-\frac{\alpha^2}{\sigma^2}\right) \end{aligned}$$

Proof. The functions $f * g$ and $\tilde{f} * g$ are both defined over R , so we employ a union-bound, bounding the probability of $|f * g - \tilde{f} * g|$ exceeding α on a given input. This multiplies the bound by a factor $|R|$.

For a fixed input $r \in R$, $|(f * g)(r) - (\tilde{f} * g)(r)| = |\epsilon_r \cdot g|$, where ϵ_r is ϵ restricted to the box $B + r \odot k$, and we are viewing ϵ_r and g as vectors in \mathbb{R}^B . We are thus led to consider $\text{Prob}(|\epsilon_r \cdot g| \geq \epsilon)$. By the rotational symmetry of the dot product, we can assume $g = (1, 0, \dots, 0)$, so that this is equal to $\text{Prob}(|\mathcal{N}(0, \sigma^2)| \geq \epsilon)$. By standard results in probability theory (the CDF of the absolute value of the normal, the so-called *half-normal*), this is $(1 - \text{erf}\left(\frac{\alpha}{\sqrt{2}\sigma}\right))$, where *erf* is the error function. Using the well-known bound

$$1 - \text{erf}(x) \leq \frac{1}{x} \frac{1}{\sqrt{2\pi}} \exp\left(-\frac{x^2}{2}\right),$$

we deduce that

$$\text{Prob}(|\mathcal{N}(0, \sigma^2)| \geq \epsilon) \leq \frac{\sigma}{\sqrt{\pi}\alpha} \exp\left(-\frac{\alpha^2}{\sigma^2}\right)$$

Multiplying by $|R|$ to obtain the union-bound, we get

$$\text{Prob}(\|f * g - \tilde{f} * g\|_\infty \geq \epsilon) \leq \frac{|R|\sigma}{\sqrt{\pi}\alpha} \exp\left(-\frac{\alpha^2}{\sigma^2}\right).$$

Next, observe that by the definition of the lower-* extension,

$$\|\widehat{f * g} - \widehat{\tilde{f} * g}\|_\infty \leq \|f * g - \tilde{f} * g\|_\infty.$$

Finally, we appeal to the standard stability result in persistence, Theorem II.1:

$$W_\infty(\widehat{\text{Diag}(f * g)}, \widehat{\text{Diag}(\tilde{f} * g)}) \leq \|\widehat{f * g} - \widehat{\tilde{f} * g}\|_\infty. \quad \square$$

Remark IV.3. Similar bounds should be attainable for other Wasserstein metrics, using, for example, χ^2 -distributions in place of the half-normal for W_2 .

We now prove the main theoretical result of the paper, for which we require some preliminary definitions and results.

Definition IV.4. For a fixed function $f : P \rightarrow \mathbb{R}^n$, we obtain a mapping ι_f of the rectangle R into $\mathbb{R}^{|B|n}$ by sending every point $r \in R$ to the vector $\{f(b + k \odot r) \mid b \in B\}$. This is technically a set, rather than a vector, but it becomes a vector after fixing an order on the elements of B . Such a mapping can be extended linearly to the entire cubical complex K_R built on top of R . Note that this extension is continuous, and generally not constant on the interior of cubes.

Lemma IV.5. *Define $\kappa = \prod_i k_i$, the product of the entries of the stride vector k . Suppose that $n\kappa \geq 2^{m+1}$. Then a generic function $f : P \rightarrow \mathbb{R}^n$ has the property that ι_f is injective on the m -skeleton K_R^m , so that $\iota_f(K_R^m)$ has the structure of a cubical complex isomorphic to K_R^m .*

Proof. Let $B^* \subseteq B$ consist of those elements in the top-left $k_1 \times k_2 \times \dots \times k_d$ corner of B . The various translates

$B^* + (k \odot r)$ are all disjoint subsets of P . We can thus view the vertices $\{f(b + k \odot r) \mid b \in B\}$ of $\iota_f(K_R^m)$ as having at least $n\kappa$ degrees of freedom, and this can be made more precise by projecting the embedding on to the coordinates corresponding to B^* . We now want to show that if we choose a collection S of points in \mathbb{R}^M for $M \geq 2^{m+1}$, and build the complete m -dimensional cubical complex on top of these points (containing all possible cubes defined by subsets of size 2^k for $k \leq m$), we will generically never have nontrivial intersections. To see this, we observe that in \mathbb{R}^M , any set of at most $M + 1$ points is generically in general position. Thus if $M \geq 2^{m+1}$, any collection of at most $2^{m+1} + 1$ points is generically in general position. We now consider three cases, assuming that all subsets of S of cardinality at most $2^{m+1} + 1$ are in general position:

- Case 1: Self-intersections. A cube of dimension k is determined by 2^k points. By translating the cube, we can assume that one of the points is zero. If the points in general position to begin with, post-translation the non-zero points will be linearly independent, and hence a self-intersection is impossible, as this amounts to having two different linear combinations be equal.
- Case 2: Intersection of two cubes whose vertex sets are not disjoint. In this case, we can translate one of the common vertices to zero, and the remaining points must again be linearly independent, so a nontrivial intersection is impossible. Note that in this case, the total number of vertices is at most $2^k + 2^k = 2^{k+1} \leq 2^{m+1}$.
- Case 3: Intersection of two cubes with disjoint vertex sets. The union of their vertex sets has cardinality $2^k + 2^k = 2^{k+1}$. Each cube lies in an affine subset of dimension $2^k - 1$, so that if these cubes intersect their union lies in an affine subset of dimension $(2^k - 1) + (2^k - 1) = 2^{k+1} - 2$, which is impossible for a collection of 2^{k+1} points in general position.

□

Definition IV.6 (Convolutional Persistence Transform). Fix $f : P \rightarrow \mathbb{R}$. The *Convolutional Persistence Transform* is the mapping $CPT(f) : \mathbb{S}^{|B|-1} \rightarrow \mathbf{Diagrams}$ that sends an L^2 -normalized function $g : B \rightarrow \mathbb{R}$ to the persistence diagram of $f * g$ on K_R^m . One can similarly define an *Euler characteristic curve* version of this invariant, the *Convolutional Euler Characteristic Transform* (CECT), by computing Euler characteristic curves instead of persistence diagrams.

Using multi-channel images $f : P \rightarrow \mathbb{R}^n$, we can define an analogous CPT and CECT. In this setting, g ranges over all L^2 -normalized functions $B \rightarrow \mathbb{R}^n$, which can be identified with $\mathbb{S}^{|B|n-1}$.

Theorem IV.7 (Generic Injectivity of CPT). *Suppose that $\kappa = \Pi_i k_i \geq 2^{m+1}$. Then the single-channel CPT and CECT are injective on a generic set of functions.*

Proof. We will show that if $f_1 \neq f_2$ are two functions for which ι_{f_1} and ι_{f_2} are injective on K_R^m , $CPT(f_1) \neq CPT(f_2)$ and $CECT(f_1) \neq CECT(f_2)$ as functions on $\mathbb{S}^{|B|-1}$. Taken together with the prior lemma, this proves the theorem.

Let f be a function such that ι_f is injective on the m -skeleton K_R^m , and hence a homeomorphism on to its image. Then for a function $g : B \rightarrow \mathbb{R}$, viewed also as a vector $\vec{g} \in \mathbb{R}^{|B|}$, observe that $(f * g)(r) = \iota_f(r) \cdot \vec{g}$ for all $r \in R$, see Figure IV.1 for a visual schematic. Thus, the filtration induced by $f * g$ on the set R (viewed as the vertex set of K_R^m) is identical to the filtration induced on $\iota_f(R)$ by the function $\langle \cdot, \vec{g} \rangle$. Since ι_f is a homeomorphism on to its image, we deduce that the lower-* filtration on K_R^m induced by $\widehat{f * g}$ is identical to the lower-* filtration on $\iota_f(K_R^m)$ given by the lower-* extension of the function $\langle \cdot, \vec{g} \rangle$ from the vertex set $\iota_f(R)$, which, by Proposition II.4, has the same persistence as the filtration on $\iota_f(K_R^m)$ given by the linear function $\langle \cdot, \vec{g} \rangle$.

Now, as \vec{g} is varied over the unit sphere in $\mathbb{R}^{|B|-1}$, the set of diagrams $PH(\iota_f(K_R^m), \langle \cdot, \vec{g} \rangle)$ is known as the *Persistent Homology Transform* (PHT) of $\iota_f(K_R^m)$ which is known to uniquely determine $\iota_f(K_R^m)$, see [TMB14, GLM18, CMT18]. Since $\iota_f(K_R^m)$ uniquely determines the function f , the collection of persistence diagrams of the form $\{PH(K_R^m, g * f) \mid g : B \rightarrow \mathbb{R}\}$, which contains the exact same information as the PHT, uniquely determines f . Injectivity of the Euler characteristic curve version of the PHT then provides injectivity for the CECT. □

Remark IV.8. What we have just shown is that having a large stride vector, in addition to providing computational speedups by lowering the resolution of the resultant grid, also provides generic injectivity for persistence of higher-dimensional data complexes.

The following corollary shows that to apply Theorem IV.7 one can ignore those filter functions orthogonal to image patches in our dataset. As [CIDSZ08] observed, the space of local patches in natural images has very high codimension in the space of all possible patches, and hence in practice the CPT may not require a very high-dimensional collection of filter functions to be effective at distinguishing images.

Definition IV.9. For a given function $f : P \rightarrow \mathbb{R}$, we say that a filter function $g : B \rightarrow \mathbb{R}$ is *convolutionally orthogonal* to f if $f * g = 0$, i.e. $(f * g)(r) = 0$ for all $r \in R$. We write f^\perp to indicate all functions convolutionally orthogonal to f .

Corollary IV.10. *Let $f_1, f_2 : P \rightarrow \mathbb{R}$ be two functions, and write $\mathcal{G} = (f_1^\perp \cap f_2^\perp)^\perp$, the orthogonal complement of the subspace of all functions convolutionally orthogonal to both f_1 and f_2 . If $\text{Diag}(\widehat{f_1 * g}) = \text{Diag}(\widehat{f_2 * g})$ for all $g \in \mathcal{G}$, then $f_1 = f_2$, and the same is true replacing persistence diagrams with Euler characteristic curves.*

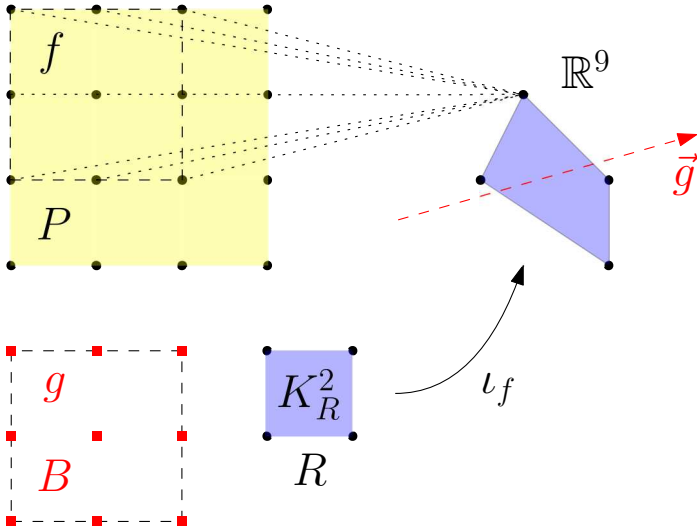


Fig. IV.1: The function f is defined on the 4×4 grid on the top left. The box B is 3×3 , and using a $(1,1)$ -stride there are four ways of laying B over the domain of f , so that R is a 2×2 grid. We can map the vertices of R into \mathbb{R}^9 by associating each vertex of R with its corresponding translate of B , and then taking as coordinates the values of f in that translate. This extends linearly to a map ι_f from the complex K_R^2 in \mathbb{R}^9 , which here is shown to be an embedding.

Proof. This follows from Theorem IV.7, noting that if f_1 and f_2 have the same persistence diagram when convolving with a function $g \in \mathcal{G}$, they also have the same diagram after convolving with $g + h$ for $h \in \mathcal{G}^\perp$. \square

Finally, we show that injectivity for the multi-channel CPT is a corollary of the injectivity for the ordinary CPT.

Corollary IV.11. *Suppose that $n\kappa = n\prod_i k_i \geq 2^{m+1}$. Then the n -channel CPT and CECT are injective on a generic set of functions.*

Proof. The embedding map ι_f of R into $\mathbb{R}^{|B|n}$ is generically injective by Lemma IV.5 when $n\kappa \geq 2^{m+1}$. By specializing to functions g of the form $g = (0, 0, \dots, g_i, \dots, 0, 0)$, the multi-channel CPT and CECT reduce to the single-channel CPT and CECT on the i -th channel f_i of the function f , which, by Theorem IV.7, determines f_i . Repeating this for each channel, we see that the multi-channel CPT and CECT determine each component of f , and hence f itself. \square

V. EXPERIMENTS

In this section, we verify experimentally the following claims: (1) convolutional persistence is considerably more informative in practice than ordinary persistence, and (2) convolutional persistence is more robust to outliers. Our aim is not to argue that persistence-based methods are superior to other methods for the tasks at hand. Nor we do try to demonstrate the computational advantages of downsampling, as this has already been shown in [SWB21b]. In all our computations, we build a simplicial complex

wherein the pixels are the top-dimensional simplices, rather than the vertices; this is the second construction in Section II-B, and is line with how the Giotto toolkit computes cubical persistence [TLT⁺21]. Code for running experiments with convolutional persistence can be found at <https://github.com/yesolomon/convpers>.

A. Classification Tasks

In what follows, we consider five datasets:

- 1) The UCI digits dataset [AK98]. The images are 8×8 . This dataset has 5620 images.
- 2) The MNIST dataset [Den12]. The images are 28×28 , and 5000 random images were chosen for the dataset.
- 3) An MNIST-like dataset of Chinese digits [NC171]. There are 15 classes, for a baseline accuracy of $1/15 \approx 0.066$. See Figure V.1 for examples. To speed up computations, a 2×2 max pooling is applied before computing persistence. The original images are 64×64 , and are 32×32 after max pooling. 5000 random images were chosen the dataset.
- 4) An MNIST-like dataset of characters in the Devanagari script [APG15]. There are 46 classes, for a baseline accuracy of $1/46 \approx 0.0217$. See Figure V.2 for examples. The images are 32×32 , and 5000 random images were chosen for the dataset.
- 5) A dataset of solutions to the *Kuramoto-Sivashinsky* PDE. This is a PDE of relevance in many systems exhibiting pattern formation [CB95, MSB12, Vil91, Wol91, GD98]. This PDE was studied in the context of topological machine learning by Adams et al. [AEK⁺17], in which they consider the anisotropic form of the PDE:

$$u_t = -\nabla^2 u - \nabla^2 \nabla^2 u + r(u_x)^2 + (u_y)^2.$$

Starting from random initial conditions, we solve these PDEs out to time $t = 15$ for a range of r values, $r \in \{1, 1.25, 1.5, 1.75, 2\}$. The classification task is then parameter estimation: giving a 2D image of the solution to the PDE, guess the r parameter that produced it. See Figure V.3 for examples. The images are 50×50 , and 500 images were generated for each r value, giving a dataset of 2500 points.

In all of our datasets, the images are small enough that the convolutions are defined to preserve the resolution, rather than downsample. The goal here is to ignore the computational advantages of convolutional persistence and focus only on the gains in discriminative power. For each dataset, we consider five versions of the CPT:

- Using a trivial 1×1 filter [1], which is equivalent to computing the persistence of the original image.
- Adding, in addition to the trivial filter, three more “standard” filters: sharpening, blur, and Gaussian kernels, all 3×3 .
- Applying PCA to the space of 3×3 image patches to obtain the top-three principal component patches,

Chinese Digit Examples

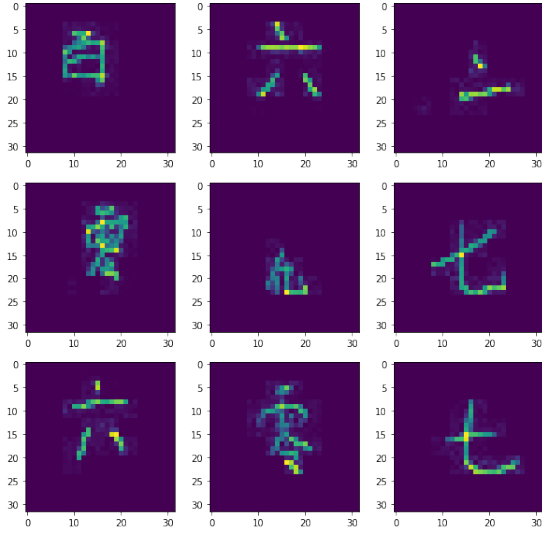


Fig. V.1: Examples of chinese digit figures.

Devanagari Script Examples

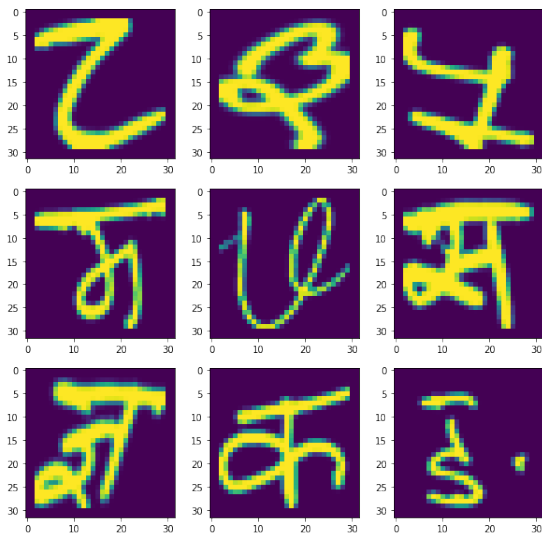


Fig. V.2: Examples of Devanagari script figures.

Kuramoto Sivanshinsky Examples

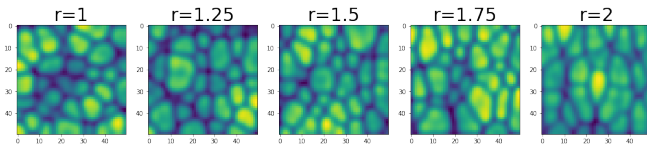


Fig. V.3: Examples of Kuramoto-Sivanshinsky figures. Note how the cells become vertically stretched for larger values of r .

and then generating five kernels as random normalized linear combinations of these patches. This approach is motivated by Corollary IV.10, which says that, for the purposes of injectivity, one can ignore filters orthogonal to those found in the patches of the dataset. We call the resulting kernels *eigenfilters*.

- Taking 5 random, normalized 3×3 filters.
- Taking 25 random, normalized 3×3 filters.

For each version of the CPT, we consider four vectorizations:

- Vectorize using persistence images (default setting, 10×10 resolution), concatenating across both homological dimensions and across filters. Thus, if there are B filters, the resulting vector has length $200B$.
- Vectorize using persistence images, as above, but average along filters rather than concatenating, giving a vector of length 200.
- Vectorize using total persistence, concatenating across both homological dimensions and across filters. Thus, if there are B filters, the resulting vector has length $2B$.
- Vectorize using total persistence, as above, but average along filters rather than concatenating, giving a vector of length 2.

Finally, for each vectorization, we test the topological features on the classification task using the following three models:

- A 3-nearest-neighbors classifier.
- Gradient boosting trees, 10 estimators.
- A neural network model with two hidden layers with 100 units each, leakyRELU activations on the hidden layers and softmax on the final layer, and adam optimizer. Trains for 50 epochs with batch size 4.

Though this series of experiments does not fully explore all the choices, applications, or features of the CPT, it is sufficiently diverse to allow for some interesting insights and the observation of recurrent patterns. Moreover, the experimental pipeline chosen is very simple and does not rely on any careful engineering of features or models.

As many components of the experimental set-up are stochastic, such as the random filters used and the initializations of the neural nets, we perform 10 simulations for each combination of experimental hyperparameters, setting aside 20% of the data as a testing set to compute model accuracy. For each choice of filters and vectorization, the model with the highest average is chosen, and the standard deviation of its accuracy across the 10 simulations is shown in the bar plot. *NN* indicates *nearest neighbors*, *Tree* is *gradient boosting trees*, and *DL* is *deep learning*, i.e. neural networks. We now consider the results:

- Digits: Convolutional persistence provides great improvements in predictive accuracy. The best results come from concatenating features rather than averaging them. Total persistence is very powerful when many random filters are used. When using only five filters, eigenfilters outperforms random filters. For this dataset, the best average

accuracies were achieved using deep learning. See Figure V.6.

- MNIST: Convolutional persistence against boosts predictive accuracy by a large margin. Similar trends to the digits dataset, although the best models are not always neural networks. See Figure V.7.
- Chinese digits: For this dataset, five eigenfilters are significantly better than five random filters. Moreover, the best vectorization is given by concatenating total persistence scores. See Figure V.8.
- Devanagari: For this dataset, taking five random filters performs about as well as taking five eigenfilters. The best average performance is given by concatenating persistence images, but similar accuracy with lower standard deviation is given by a nearest neighbor classifier on the concatenated total persistence vectors. See Figure V.9.
- Kuramoto-Sivashinsky: The advantages of convolutional persistence are evident but less dramatic. As in the prior two experiments, the concatenated total persistence vectors for 25 random filters is significantly more informative than any vectorizations of ordinary persistence. Better performance (over 95%!) is possible using neural networks on the concatenated persistence image vector, but this is less stable to some of the experimental hyperparameters. See Figure V.10.

B. Robustness Experiment

In this experiment, we aim to show that convolutional persistence is more robust than ordinary persistence. Our experimental design is the following. We use the UCI digits dataset [AK98], but due to the small resolution of these images, we upsample them via cubic spline interpolation from 8×8 to be 64×64 . We consider the effect on persistence of perturbing these images, and we distinguish between two kinds of deformations: *noisy deformations* that consist of adding pixelwise Gaussian noise, and *tangent deformations* that consists of moving an image along a line connecting it to another image in the data set. To be precise, the Gaussian noise ϵ will be pixelwise iid $\mathcal{N}(0, 0.001)$, and a tangent deformation of an image X will be $v = \frac{Y-X}{1000}$, where Y is another image randomly selected from the dataset. We will compare the persistence diagrams of X with those of $X + \epsilon$ and $X + v$ for 5000 randomly chosen triples (X, ϵ, v) , and normalize the resulting diagram distances by $\|\epsilon\|_\infty$ and $\|v\|_\infty$. To justify the claim that convolutional persistence is more robust, we would like it to be more stable to noisy deformations but still sensitive to tangent deformations. Indeed, it is trivial to create an invariant that is more stable to all deformations, simply by rescaling the original invariant by a constant smaller than one; the value of a robust invariant is that it can overlook noise but detect meaningful differences.

Convolutional persistence has the flexibility of allowing the user to pick the filters to be used. In this setting, we use the eigenfilters approach considered in the prior experiment. That is, we perform PCA on the space of 10×10 patches

Topological Distortion of iid Gaussian Noise

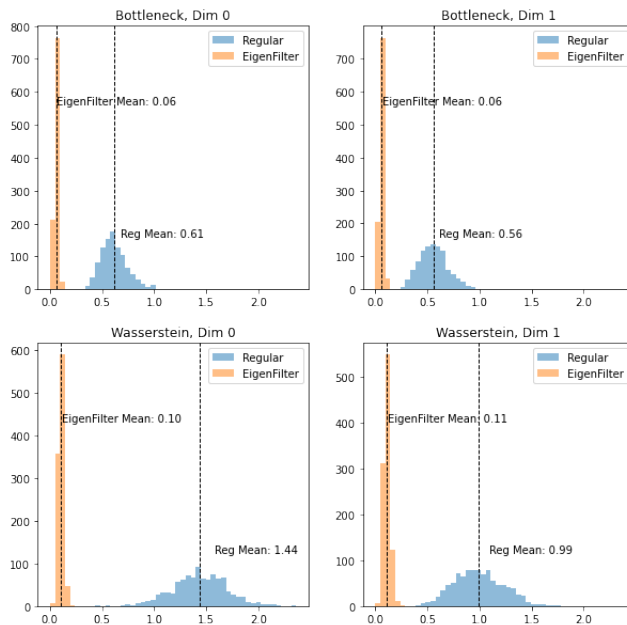


Fig. V.4: Comparing robustness of ordinary and convolutional persistence with respect to Gaussian noise. We see that average perturbation is typically about a factor of 10 smaller for convolutional persistence.

in the image set, keep the top three largest eigenpatches, and consider random linear combinations of these eigenpatches, normalized in the L^1 norm as suggested by Proposition IV.1. We use larger patches here than in the classification experiments in order to highlight the robustness phenomenon, which improves with the size of the patches used and is therefore particularly effective for high-resolution images. Similar but less dramatic results are obtained using smaller patches.

There is also a choice to be made for how measure distances between diagrams; we consider both Bottleneck and 2-Wasserstein distances, separating out the calculations for degrees 0 and 1 of persistence. The results are shown in Figures V.4 and V.5. We see that convolutional persistence is considerably more robust to noise than ordinary persistence, but that this effect is significantly reduced when the deformations lie within the data subspace.

C. Observations & Discussion

We conclude this experimental section with a few comments.

- Random filters consistently work well at providing informative features, although there is little theoretical justification for why this should be the case. It is possible that this is related to Johnson-Lindenstrauss theory [Lin84].

Topological Distortion of Tangent Deformations

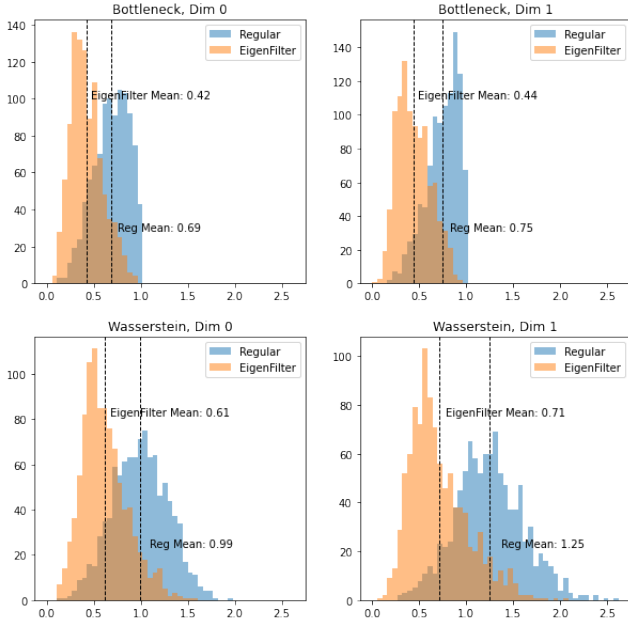


Fig. V.5: Comparing robustness of ordinary and convolutional persistence with respect to tangent deformations. We see that average perturbation for convolutional persistence is at least half of that of ordinary persistence.

- It is also surprising that total persistence is such an effective vectorization across multiple experiments, despite being so reductive.
- Given that eigenfilters tend to outperform random filters, it would be interesting (and easy) to compare 25 random linear combinations of eigenfilters with 25 random filters.
- In our eigenfilters experiments, we opt for taking multiple random combinations of the top eigenfilters, rather than using the eigenfilters themselves, and taking more of them. This was based on some theoretical heuristics and small-scale experiments, but there is otherwise no reason to suggest why one approach is generally superior to the other.
- We did not apply any feature engineering before applying our machine learning models. For example, the concatenated persistence images vectors were fairly large, 5000-dimensional in the case of 25 random filters, and performance might be improved by pre-applying a dimensionality reduction method like PCA.
- Similarly, we did not do any engineering of our machine learning models, fixing a simple neural network architecture across all experiments. For the Kuramoto-Sivashinsky PDE dataset, the high variance of the neural network models suggests that significantly improved performance might be achievable using the right architecture and training regime.
- Another hyper-parameter we did not test extensively is

Digits Dataset

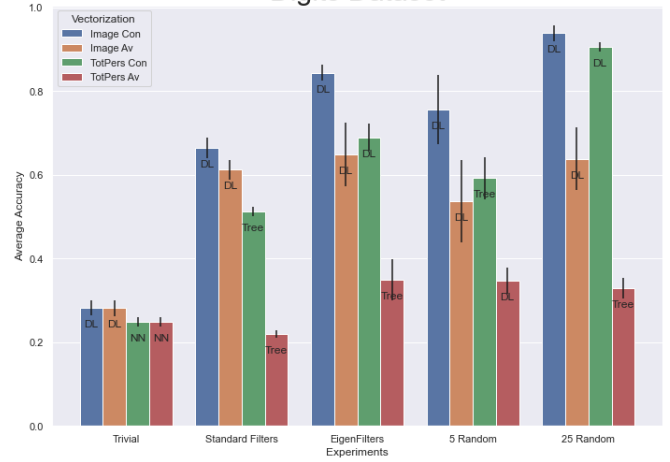


Fig. V.6: Results for the digits dataset.

MNIST Dataset

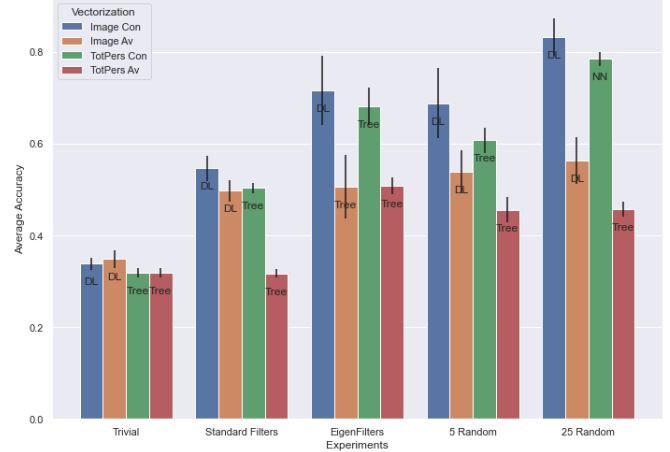


Fig. V.7: Results for the MNIST dataset.

the size of the filters. Some preliminary experiments suggest that 4×4 filters outperform the 3×3 filters used here, but it remains to be seen if this phenomenon is robust.

VI. CONCLUSION

In this paper, we have proposed a novel approach to topological analysis of images, based on combining convolutions and persistent homology. Packaging this invariant as a topological transform, we have shown that this transform is injective in a generic sense by viewing it as a special case of the persistent homology transform. We have also provided diverse experiments showing that convolutions are effective at improving the predictive power of persistent homology for classification tasks. Looking forward, there are multiple directions for future research.

- The injectivity theory for the PHT has been extended by results bounding the number of vector directions needed to obtain injectivity for certain classes of shapes,

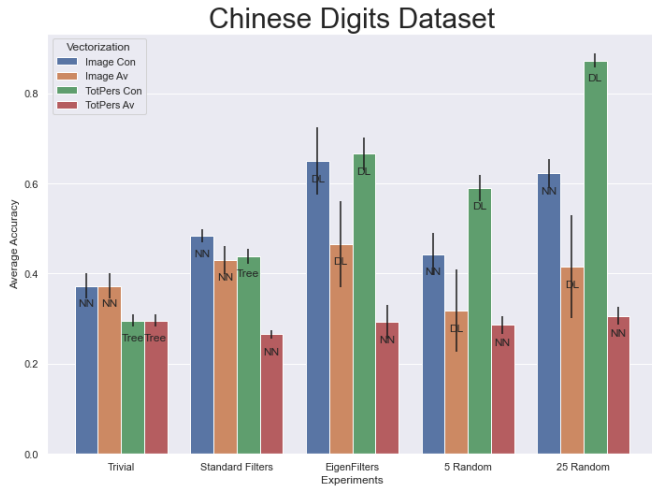


Fig. V.8: Results for the chinese digits dataset.

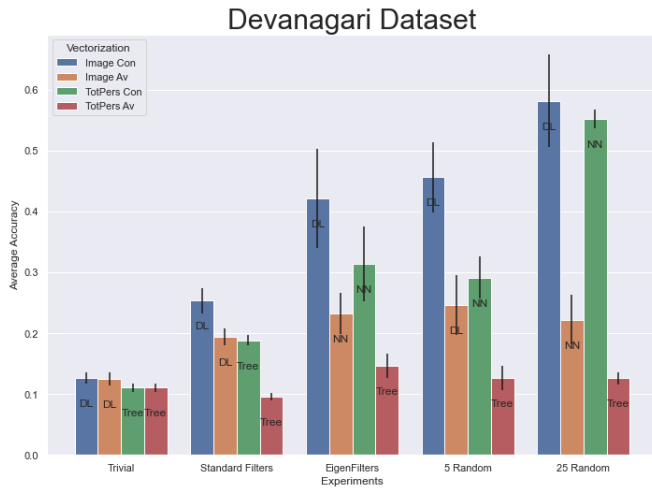


Fig. V.9: Results for the Devanagari dataset.

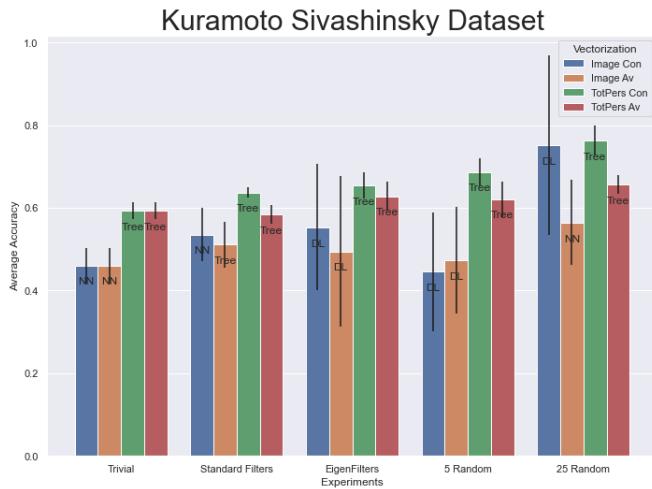


Fig. V.10: Results for the Kuramoto-Sivashinsky dataset.

see [CMT18, BFM⁺18, FMM⁺19, BFM⁺20]. It would be interesting to try and obtain similar, specialized results for the embedded cubical complexes appearing in this paper.

- As of yet, there are no *inverse stability* results for the PHT, as were obtained for the topological transform in [SWB21a]. That is, the regularity of the inverse map from topological features to shapes has not been investigated. It is possible that the restricted, discrete structure of the CPT provides an easier setting for studying this question.
- We did not consider a pipeline in which the convolutional filters are trainable parameters learned using the dataset. This is entirely possible, see [CCG⁺21, SWB21b], but presents multiple computational challenge, as topological optimization is expensive and unstable, and the topological energy landscape has many poor local minima. Still, this is an interesting direction for future work.
- We considered persistence images and total persistence as vectorizations in our experimental pipeline. Other possible vectorizations include persistence landscapes [Bub15] and Euler characteristic curves.
- The datasets explored here, though not synthetic, are fairly simplistic, and such classification tasks have been *solved* by deep learning methods which surpasses human accuracy [RDS⁺15]. A natural next step is to consider more challenging settings, particularly in the data-starved regime, where topological features have proved useful [KZWB22] for obtaining start-of-the-art performance, and see if convolutional persistence can further boost the accuracy of such models.
- Finally, it would be interesting to experiment with multi-channel images (e.g. RGB α) as well as 3D images (as often arise in medical imaging), and study the impact of convolutional persistence in this setting.

REFERENCES

- [ACC⁺20] Andrew Aukerman, Mathieu Carrière, Chao Chen, Kevin Gardner, Raúl Rabadán, and Rami Vanguri, *Persistent homology based characterization of the breast cancer immune microenvironment: a feasibility study*, 36th international symposium on computational geometry (socg), 2020. \uparrow 1
- [AEK⁺17] Henry Adams, Tegan Emerson, Michael Kirby, Rachel Neville, Chris Peterson, Patrick Shipman, Sofya Chepushtanova, Eric Hanson, Francis Motta, and Lori Ziegelmeier, *Persistence images: A stable vector representation of persistent homology*, Journal of Machine Learning Research **18** (2017). \uparrow 1, 9
- [AK98] E Alpaydin and C Kaynak, *Optical recognition of handwritten digits data set*, UCI Machine Learning Repository (1998). \uparrow 9, 11
- [APG15] Shailesh Acharya, Ashok Kumar Pant, and Prashna Kumar Gyawali, *Deep learning based large scale handwritten devanagari character recognition*, 2015 9th international conference on software, knowledge, information management and applications (skima), 2015, pp. 1–6. \uparrow 9
- [BB97] Mladen Bestvina and Noel Brady, *Morse theory and finiteness properties of groups*, Inventiones mathematicae **129** (1997), no. 3, 445–470. \uparrow 5
- [BBW20] Paul Bendich, Peter Bubenik, and Alexander Wagner, *Stabilizing the unstable output of persistent homology computations*, Journal of Applied and Computational Topology **4** (2020), no. 2, 309–338. \uparrow 5

- [BCD⁺14] Mickaël Buchet, Frédéric Chazal, Tamal K Dey, Fengtao Fan, Steve Y Oudot, and Yusu Wang, *Topological analysis of scalar fields with outliers*, arXiv preprint arXiv:1412.1680 (2014). †5
- [BFM⁺18] Robin Lynne Belton, Brittany Terese Fasy, Rostik Mertz, Samuel Micka, David L Millman, Daniel Salinas, Anna Schenfish, Jordan Schupbach, and Lucia Williams, *Learning simplicial complexes from persistence diagrams*, arXiv preprint arXiv:1805.10716 (2018). †13
- [BFM⁺20] Robin Lynne Belton, Brittany Terese Fasy, Rostik Mertz, Samuel Micka, David L Millman, Daniel Salinas, Anna Schenfish, Jordan Schupbach, and Lucia Williams, *Reconstructing embedded graphs from persistence diagrams*, Computational Geometry **90** (2020), 101658. †13
- [BGH⁺21] Bea Bleile, Adélie Garin, Teresa Heiss, Kelly Maggs, and Vanessa Robins, *The persistent homology of dual digital image constructions*, arXiv preprint arXiv:2102.11397 (2021). †4
- [BL22] Magnus Bakke Botnan and Michael Lesnick, *An introduction to multiparameter persistence*, arXiv preprint arXiv:2203.14289 (2022). †5
- [BR07] Vladimir Igorevich Bogachev and Maria Aparecida Soares Ruas, *Measure theory*, Vol. 1, Springer, 2007. †7
- [Bub15] Peter Bubenik, *Statistical topological data analysis using persistence landscapes.*, J. Mach. Learn. Res. **16** (2015), no. 1, 77–102. †1, 13
- [BW20] Peter Bubenik and Alexander Wagner, *Embeddings of persistence diagrams into hilbert spaces*, Journal of Applied and Computational Topology **4** (2020), no. 3, 339–351. †1
- [Car09] Gunnar Carlsson, *Topology and data*, Bulletin of the American Mathematical Society **46** (2009), no. 2, 255–308. †2
- [CB95] Rodolfo Cuerno and Albert-László Barabási, *Dynamic scaling of ion-sputtered surfaces*, Physical review letters **74** (1995), no. 23, 4746. †9
- [CCG⁺21] Mathieu Carriere, Frédéric Chazal, Marc Glisse, Yuichi Ike, Hariprasad Kannan, and Yuhei Umeda, *Optimizing persistent homology based functions*, International conference on machine learning, 2021, pp. 1294–1303. †5, 13
- [CD18] Yu-Min Chung and Sarah Day, *Topological fidelity and image thresholding: A persistent homology approach*, Journal of Mathematical Imaging and Vision **60** (2018), no. 7, 1167–1179. †1
- [CDH22] Yu-Min Chung, Sarah Day, and Chuan-Shen Hu, *A multi-parameter persistence framework for mathematical morphology*, Scientific reports **12** (2022), no. 1, 1–25. †1
- [CG21] Sabrina S Calcina and Marcio Gameiro, *Parameter estimation in systems exhibiting spatially complex solutions via persistent homology and machine learning*, Mathematics and Computers in Simulation **185** (2021), 719–732. †1
- [CIDSZ08] Gunnar Carlsson, Tigran Ishkhanov, Vin De Silva, and Afra Zomorodian, *On the local behavior of spaces of natural images*, International journal of computer vision **76** (2008), no. 1, 1–12. †8
- [CMC⁺20] Lorin Crawford, Anthea Monod, Andrew X Chen, Sayan Mukherjee, and Raúl Rabadán, *Predicting clinical outcomes in glioblastoma: an application of topological and functional data analysis*, Journal of the American Statistical Association **115** (2020), no. 531, 1139–1150. †1
- [CMT18] Justin Curry, Sayan Mukherjee, and Katharine Turner, *How many directions determine a shape and other sufficiency results for two topological transforms*, arXiv preprint arXiv:1805.09782 (2018). †6, 8, 13
- [COO15] Mathieu Carrière, Steve Y Oudot, and Maks Ovsjanikov, *Stable topological signatures for points on 3d shapes*, Computer graphics forum, 2015, pp. 1–12. †1
- [CSEH07] David Cohen-Steiner, Herbert Edelsbrunner, and John Harer, *Stability of persistence diagrams*, Discrete & computational geometry **37** (2007), no. 1, 103–120. †4
- [Cur18] Justin Curry, *The fiber of the persistence map for functions on the interval*, Journal of Applied and Computational Topology **2** (2018), no. 3, 301–321. †5
- [Den12] Li Deng, *The mnist database of handwritten digit images for machine learning research [best of the web]*, IEEE signal processing magazine **29** (2012), no. 6, 141–142. †9
- [DFF15] Barbara Di Fabio and Massimo Ferri, *Comparing persistence diagrams through complex vectors*, International conference on image analysis and processing, 2015, pp. 294–305. †1
- [EH10] Herbert Edelsbrunner and John Harer, *Computational topology: an introduction* (2010). †2, 5
- [FMM⁺19] Brittany Terese Fasy, Samuel Micka, David L Millman, Anna Schenfish, and Lucia Williams, *Persistence diagrams for efficient simplicial complex reconstruction*, arXiv preprint arXiv:1912.12759 **1** (2019), 5. †13
- [GD98] Alexander A Golovin and Stephen H Davis, *Effect of anisotropy on morphological instability in the freezing of a hypercooled melt*, Physica D: Nonlinear Phenomena **116** (1998), no. 3–4, 363–391. †9
- [GHO16] Marcio Gameiro, Yasuaki Hiraoka, and Ippei Obayashi, *Continuation of point clouds via persistence diagrams*, Physica D: Nonlinear Phenomena **334** (2016), 118–132. †5
- [Ghr08] Robert Ghrist, *Barcodes: the persistent topology of data*, Bulletin of the American Mathematical Society **45** (2008), no. 1, 61–75. †2
- [GLM18] Robert Ghrist, Rachel Levanger, and Huy Mai, *Persistent homology and euler integral transforms*, Journal of Applied and Computational Topology **2** (2018), no. 1, 55–60. †6, 8
- [HLSC19] Xiaoling Hu, Fuxin Li, Dimitris Samaras, and Chao Chen, *Topology-preserving deep image segmentation*, Advances in neural information processing systems **32** (2019). †1
- [HNNH⁺16] Yasuaki Hiraoka, Takenobu Nakamura, Akihiko Hirata, Emerson G Escolar, Kaname Matsue, and Yasumasa Nishiura, *Hi-erarchical structures of amorphous solids characterized by persistent homology*, Proceedings of the National Academy of Sciences **113** (2016), no. 26, 7035–7040. †1
- [JKN20] Qitong Jiang, Sebastian Kurtek, and Tom Needham, *The weighted euler curve transform for shape and image analysis*, Proceedings of the IEEE/CVF conference on computer vision and pattern recognition workshops, 2020, pp. 844–845. †6
- [KKZ⁺20] Kwangho Kim, Jisu Kim, Manzil Zaheer, Joon Kim, Frédéric Chazal, and Larry Wasserman, *Pllay: Efficient topological layer based on persistent landscapes*, Advances in Neural Information Processing Systems **33** (2020), 15965–15977. †7
- [KMM04] Tomasz Kaczynski, Konstantin Michael Mischaikow, and Marian Mrozek, *Computational homology*, Vol. 3, Springer, 2004. †3
- [KZWB22] Ekaterina Khramtsova, Guido Zuccon, Xi Wang, and Mahsa Baktashmotlagh, *Rethinking persistent homology for visual recognition*, arXiv e-prints (2022), arXiv:2207. †1, 13
- [LCO18] Théo Lacombe, Marco Cuturi, and Steve Oudot, *Large scale computation of means and clusters for persistence diagrams using optimal transport*, Advances in Neural Information Processing Systems **31** (2018). †4
- [LHP21] Jacob Leygonie and Gregory Henselman-Petrusek, *Algorithmic reconstruction of the fiber of persistent homology on cell complexes*, arXiv preprint arXiv:2110.14676 (2021). †5
- [Lin84] W Johnson Lindenstrauss, *Extensions of lipschitz maps into a hilbert space*, Contemp. Math **26** (1984), no. 189–206, 2. †11
- [LT21] Jacob Leygonie and Ulrike Tillmann, *The fiber of persistent homology for simplicial complexes*, arXiv preprint arXiv:2104.01372 (2021). †5
- [MKPGC19] Anthea Monod, Sara Kalisnik, Juan Ángel Patino-Galindo, and Lorin Crawford, *Tropical sufficient statistics for persistent homology*, SIAM Journal on Applied Algebra and Geometry **3** (2019), no. 2, 337–371. †1
- [MMS11] Nikola Milosavljević, Dmitriy Morozov, and Primož Skraba, *Zigzag persistent homology in matrix multiplication time*, Proceedings of the twenty-seventh annual symposium on computational geometry, 2011, pp. 216–225. †1, 4
- [MOS19] Clément Maria, Steve Oudot, and Elchanan Solomon, *Intrinsic topological transforms via the distance kernel embedding*, arXiv preprint arXiv:1912.02225 (2019). †6
- [MSB12] Francis C Motta, Patrick D Shipman, and R Mark Bradley, *Highly ordered nanoscale surface ripples produced by ion bombardment of binary compounds*, Journal of Physics D: Applied Physics **45** (2012), no. 12, 122001. †9
- [NC171] K Nazarpour and M Chen, *Handwritten Chinese Numbers* (2017). †9
- [OPT⁺17] Nina Otter, Mason A Porter, Ulrike Tillmann, Peter Grindrod, and Heather A Harrington, *A roadmap for the computation of persistent homology*, EPJ Data Science **6** (2017), 1–38. †4

- [OS17] Steve Oudot and Elchanan Solomon, *Barcode embeddings for metric graphs*, arXiv preprint arXiv:1712.03630 (2017). ↑6
- [OS20] Steve Oudot and Elchanan Solomon, *Inverse problems in topological persistence*, Topological data analysis, 2020, pp. 405–433. ↑6
- [Oud15] Steve Y Oudot, *Persistence theory: from quiver representations to data analysis*, Vol. 209, American Mathematical Society Providence, 2015. ↑2
- [Oud17] Steve Y Oudot, *Persistence theory: from quiver representations to data analysis*, Vol. 209, American Mathematical Soc., 2017. ↑4
- [PSO18] Adrien Poulenard, Primoz Skraba, and Maks Ovsjanikov, *Topological function optimization for continuous shape matching*, Computer graphics forum, 2018, pp. 13–25. ↑5
- [RDS⁺15] Olga Russakovsky, Jia Deng, Hao Su, Jonathan Krause, Sanjeev Satheesh, Sean Ma, Zhiheng Huang, Andrej Karpathy, Aditya Khosla, and Michael Bernstein, *Imagenet large scale visual recognition challenge*, International journal of computer vision **115** (2015), no. 3, 211–252. ↑13
- [SMM⁺21] Anna Suzuki, Miyuki Miyazawa, James M Minto, Takeshi Tsuji, Ippei Obayashi, Yasuaki Hiraoka, and Takatoshi Ito, *Flow estimation solely from image data through persistent homology analysis*, Scientific reports **11** (2021), no. 1, 1–13. ↑1
- [ST20] Primoz Skraba and Katharine Turner, *Wasserstein stability for persistence diagrams*, arXiv preprint arXiv:2006.16824 (2020). ↑5
- [SWB21a] Elchanan Solomon, Alexander Wagner, and Paul Bendich, *From geometry to topology: Inverse theorems for distributed persistence*, arXiv preprint arXiv:2101.12288 (2021). ↑13
- [SWB21b] Yitzchak Solomon, Alexander Wagner, and Paul Bendich, *A fast and robust method for global topological functional optimization*, International conference on artificial intelligence and statistics, 2021, pp. 109–117. ↑6, 7, 9, 13
- [SWB22] Elchanan Solomon, Alexander Wagner, and Paul Bendich, *From Geometry to Topology: Inverse Theorems for Distributed Persistence*, 38th international symposium on computational geometry (socg 2022), 2022, pp. 61:1–61:16. ↑6
- [TLT⁺21] Guillaume Tautzin, Umberto Lupo, Lewis Tunstall, Julian Burrella Pérez, Matteo Caorsi, Anibal M Medina-Mardones, Alberto Dassatti, and Kathryn Hess, *giotto-tda: A topological data analysis toolkit for machine learning and data exploration.*, J. Mach. Learn. Res. **22** (2021), no. 39, 1–6. ↑9
- [TMB14] Katharine Turner, Sayan Mukherjee, and Doug M Boyer, *Persistent homology transform for modeling shapes and surfaces*, Information and Inference: A Journal of the IMA **3** (2014), no. 4, 310–344. ↑2, 6, 8
- [Vil21] Cédric Villani, *Topics in optimal transportation*, Vol. 58, American Mathematical Soc., 2021. ↑4
- [Vil91] J Villain, *Continuum models of crystal growth from atomic beams with and without desorption*, Journal de physique I **1** (1991), no. 1, 19–42. ↑9
- [Wag21] Alexander Wagner, *Nonembeddability of persistence diagrams with p_{ζ}^2 wasserstein metric*, Proceedings of the American Mathematical Society **149** (2021), no. 6, 2673–2677. ↑1
- [Wol91] Dietrich E Wolf, *Kinetic roughening of vicinal surfaces*, Physical review letters **67** (1991), no. 13, 1783. ↑9